Torque force in the kinesin stroke drives coupled yaw axis and orbital rotations of kinesin coated gold nanorods

Mitsuhiro Sugawa[a,b,*], Yohei Maruyama[a], Masahiko Yamagishi[a], Robert A. Cross[c] and Junichiro Yajima[a,b,d,*]

[a]Department of Life Sciences, Graduate School of Arts and Sciences, The University of Tokyo, 3-8-1, Komaba, Meguro-ku, Tokyo 153-8902, Japan

[b]Komaba Institute for Science, The University of Tokyo, 3-8-1, Komaba, Meguro-ku, Tokyo 153-8902, Japan

[c]Center for Mechanochemical Cell Biology, Warwick Medical School, Coventry, CV4 7AL, UK

[d]Research Center for Complex Systems Biology, The University of Tokyo, 3-8-1, Komaba, Meguro-ku, Tokyo 153-8902, Japan

[*]To whom correspondence should be addressed:

mitsuhiro-sugawa@g.ecc.u-tokyo.ac.jp, yajima@bio.c.u-tokyo.ac.jp

Author contributions

M.S. and J.Y. designed research; M.S. performed research; M.S., Y.M., and M.Y. contributed new reagents/analytic tools; M.S. analyzed data and performed simulations; M.S., R.A.C. and J.Y. wrote the paper.

ABSTRACT

Kinesin motor domains generate impulses of force and movement that have both translational and rotational components, raising the question of how the rotational component contributes to motor function. We used a new assay in which kinesin-coated gold nanorods (kinesin-GNRs) move on suspended microtubules, for three plus-end-directed kinesins: single-headed KIF1A, dimeric ZEN-4 and single-headed kinesin-1. Polarization of the light scattered by all three types of kinesin-GNRs periodically oscillated as they orbited the microtubule along a left-handed helical trajectory. Our analyses revealed that each kinesin-GNR unidirectionally rotates about its yaw axis as it translocates, and that the period of this yaw-axis rotation corresponds to two periods of its left-handed helical orbit around the microtubule axis. Stochastic simulations suggest that the yaw-axis rotation enhances biased lateral displacement of the kinesin team. Our study reveals biaxial rotation as a new mode of motility in kinesin teams that helps the team to sidestep obstacles.

36 **MAIN TEXT**

37 Kinesins are adenosine 5'-triphosphate (ATP)-driven and microtubule-based molecular
38 motors with multiple mechanical functions, including cargo transport along microtubules,
39 the regulation of microtubule dynamics, and the sliding of bundled microtubules[1–3].
40 Recent advances in techniques for 3D particle tracking with simultaneous measurements
41 of force and torque have revealed that kinesins have translational and rotational degrees
42 of freedom on microtubules, such that their motilities consist of both helical[4–8] and
43 rotational[9] motions. For example, single-molecule kinesin-1 dimers unidirectionally
44 rotate their stalk domain as they move processively via a hand-over-hand mechanism,
45 especially at high ATP concentration[9]. Furthermore, mutagenic elongation of the neck
46 linker of kinesin-1 dimers increases the probability of protofilament switching during
47 stepping along the microtubule[10]. The neck-linker mutant dimers retain processivity but
48 switch protofilaments more readily, driving left-handed helical motion of multimotor-
49 coated beads around the axis of the microtubule, whereas individual wild-type kinesin-1
50 dimers faithfully track the microtubule axis by stepping along individual protofilaments[6].
51 The protofilament-tracking ability of kinesin-1 dimers may derive from their rotary hand-
52 over-hand mechanism[9] and their neck stability[6,8]. Wild-type kinesin-2 and -8, which have
53 longer neck-linker domains than kinesin-1, and kinesin-6, which has an atypical neck
54 region, do not track protofilaments. All these kinesins move towards microtubule plus
55 ends along left-handed helical trajectories, as shown in a bead assay[6,11], a microtubule
56 surface-gliding assay[8,11–13], and a single-molecule tracking assay[8]. Furthermore, teams of
57 non-processive dimeric kinesin-14 Ncd[14–16], which moves towards microtubule minus

58 ends, as well as teams of truncated single-headed kinesins-1[17,18], -3[19], -5[4,20] and -6[11]
59 motors have all been shown to drive corkscrewing motions of microtubules in surface-
60 gliding assays. The handedness of these motions is consistent. Whilst plus-end directed
61 kinesins move along a left-handed helix, minus-ended kinesins move along a right-
62 handed helix. These helical motilities imply that the stroke (the unitary impulse of force
63 and movement generated by the motor domains) has an off axis (torque) component,
64 driven either by conformational changes in the motor domain or by the directionally
65 biased selection of microtubule binding sites[6,8,11,15,17,19] (or potentially both). The
66 underlying mechanisms and functional relevance of the torque component remain elusive.
67 To gain further insight, we have developed a novel motility assay in which gold
68 nanorods (GNRs), coated with a team of kinesin molecules, move unhindered along
69 suspended microtubules. Our assay uses light scattered by the kinesin-coated GNRs to
70 track their position, and the polarization of the light that they scatter to report their
71 orientation. We performed the GNR motility assay on three plus-end-directed kinesins:
72 single-headed KIF1A, dimeric ZEN-4 and single-headed kinesin-1.

Results

GNR imaging for particle tracking and polarization measurements. We developed a motility assay based on tracking of kinesin-coated GNRs. Focusing of light scattered by the GNRs allows positional tracking, whilst the ratio of the polarization of this scattered light in orthogonal directions reports the orientation of the GNR as it moves over the microtubule surface (Fig. 1a and Methods). GNR images were obtained by laser dark-field imaging using highly inclined illumination with nearly total internal reflection angle[21,22] via a perforated dichroic mirror[23]. The position of each GNR spot was measured in three dimensions using a cylindrical lens[24] (Fig. S1). Polarization measurements of GNRs were performed using a combination of the polarized incident laser beam and a polarizing beam displacer, which two orthogonal polarization signals were projected on the camera, allowing us to measure 0° to 180° GNR orientations in the sample plane (Fig. 1b and Methods). Kinesin constructs were prepared with a biotinylated peptide (Avi-tag) fused to their C-terminus. Biotinylated GNRs (40 nm × 68 nm) were coated in streptavidin and biotinylated kinesin molecules were attached to this streptavidin layer (Methods). Maximum capacity of kinesin molecules attached to the GNR is roughly estimated to be ~100 molecules and a portion of the attached kinesin molecules could generate driving force and torque on the microtubule. Microtubules were suspended on microbeads (0.5 μm) via the antigen–antibody system for β-tubulin, so that kinesin-coated GNRs were free to orbit the microtubules between bead-attachment points (Fig. 1c). Control experiments established that the *Z*-displacement of GNR in the range of ±200 nm had negligible effect on the GNR polarization measurement in our experimental system

95 (Fig. S2). Using the GNR motility assay, we performed a comparative analysis of three
96 plus-end-directed kinesins, which have distinctive properties of processivity and
97 oligomeric state: biased-diffusional motile and single-headed human kinesin-3 (KIF1A)[25],
98 weakly processive and dimeric *Caenorhabditis elegans* kinesin-6 (ZEN-4)[26], and non-
99 processive and truncated single-headed rat kinesin-1 (KIF5B)[27] (Methods).
100
101 **GNR motility assay for single-headed KIF1A.** We performed the GNR motility assay
102 for single-headed KIF1A (1-366 amino acid residues (AAs))[25] at a saturating ATP
103 concentration (2 mM ATP). GNRs carried multiple KIF1A molecules, allowing GNRs to
104 move processively along microtubules. We found that the light-scattering intensities of
105 each pair of KIF1A-coated GNR (KIF1-GNR) spots, corresponding to orthogonal
106 polarization signals from a single GNR, periodically oscillated in intensity during helical
107 movement, with an increase in each signal corresponding to a decrease in the other (13
108 particles out of 62 tested KIF1-GNRs) (Fig. 1d and Supplementary movie 1). The degree
109 of polarization (DOP) as a function of the summed-intensity of the two GNR spots
110 depicted an elliptical trajectory, indicating continuous rotations of the polarization (Fig.
111 1e). The *X*–*Y*–*Z*-trajectory of the KIF1-GNR showed steady left-handed helical motion
112 around the microtubule long axis (Fig. 1f). Figure 1g shows that the time trajectories of
113 the *X*- and *Y*-displacements, the degree of polarization and summed-intensity, and the
114 polarization angle as viewed from above the glass substrate. The time trajectory of the
115 polarization angle exhibited continuous counterclockwise rotations during the left-
116 handed helical motion of the KIF1-GNR around the microtubule. The *Y*-displacement and

117 the polarization signals of the KIF1-GNR exhibited strong cross-correlation and
118 periodicity (Fig. 1h), indicating that the GNR polarization fluctuation was synchronized
119 with the helical motion on the microtubule. We also observed clockwise and oscillatory
120 rotations of the GNR polarization, synchronized with the helical motion of KIF1-GNRs
121 (Fig. 2a and 2b). The translational velocity (parallel to the microtubule axis) was 0.51 ±
122 0.12 μm s^{-1} (mean ± standard deviation (SD), n = 13 GNRs), which is nearly equal to the
123 microtubule sliding velocity of 0.49 μm s^{-1} in the surface-gliding assay (Fig. S3). The
124 pitch of the helical motion measured in the X–Y-trajectory was 0.69 ± 0.36 μm (mean ±
125 SD, n = 33 cycles in 13 KIF1-GNRs), which is slightly shorter than that of the
126 corkscrewing of microtubules on a surface of KIF1A of 0.89 ± 0.21 μm (mean ± SD, n =
127 35 cycles in 5 microtubules) ($p \ll 0.01$, Welch's t-test). The displacement in the
128 microtubule axis during one cycle of fluctuation of the GNR polarization signals
129 (hereafter referred to as polarization pitch) was 0.69 ± 0.37 μm (mean ± SD, n = 33 cycles
130 in 13 KIF1-GNRs), which was almost equal to that of the helix pitch (Fig. 2c). We note
131 that the measured helix pitch is a combination of the helix pitch exerted by motors on the
132 straight microtubule lattice and any supertwist pitch of the microtubule, with the
133 supertwist depending on the number of the protofilaments. However, when the measured
134 helix pitch is less than 1 μm, as it is here, the supertwist of the microtubule has negligible
135 influence on the measured helix pitch (Methods and Fig. S4). We therefore report the
136 uncorrected helix pitch unless otherwise mentioned.
137
138 **GNR motility assay for dimeric ZEN-4 and single-headed kinesin-1.** Next, we

139 performed the GNR motility assay for the weakly-processive dimeric kinesin, ZEN-4 (1-
140 555 AAs)[26], again at a saturating ATP concentration (2 mM) (Methods). We again found
141 that the polarization signals of the ZEN4-coated GNRs (ZEN4-GNR) periodically
142 changed, correlated with the *Y*-displacements during steady forward movement (13
143 particles out of 49 tested ZEN4-GNRs) (Fig. 3a). The analyses revealed the counter-
144 clockwise, clockwise, and oscillatory rotations of these ZEN4-GNRs. The forward
145 velocity of the ZEN4-GNR was 0.39 ± 0.05 μm s^{-1} (mean ± SD, n = 13 ZEN4-GNRs),
146 which is comparable to the velocity in the bead assay[11]. The polarization pitch of the
147 ZEN4-GNR was 0.67 ± 0.20 μm (mean ± SD, n = 34 cycles in 13 ZEN4-GNRs) in the
148 microtubule axis, which is equal to the helix pitch of 0.67 ± 0.21 μm (mean ± SD, n = 34
149 cycles in 13 ZEN4-GNRs) (Fig. 3b). Thus, whilst ZEN4-GNRs moved more slowly than
150 KIF1-GNRs, the polarization rotation of ZEN4-GNRs was again phase-locked to their
151 helical motion, as for KIF1-GNRs.

152 Lastly, we also performed the GNR motility assay for the non-processive truncated
153 single-headed kinesin-1 (sK1) (1-340 AAs)[27] and the processive double-headed kinesin-
154 1 (dK1) (1-430 AAs)[27] constructs at a saturating ATP concentration (2 mM) for
155 comparison with the experiments of the single-headed and biased-diffusional motile
156 KIF1A and the double-headed and weakly processive ZEN-4. For sK1 GNRs, we again
157 found examples where the light-scattering intensities of each orthogonally polarized pair
158 of spots changed periodically during steady forward movement (5 particles out of 40
159 tested sK1-GNRs) (Fig. 3c). The forward velocity of sK1-GNRs was 0.21 ± 0.02 μm s^{-1}
160 (mean ± SD, n = 5 sK1-GNRs), which is comparable to previously reported velocities in

161 the bead assay[28]. The polarization pitch of the sK1-GNR was 0.83 ± 0.19 μm (mean ±
162 SD, n = 11 cycles in 5 sK1-GNRs), which is again comparable to the helix pitch of 0.80
163 ± 0.21 μm (mean ± SD, n = 11 cycles in 5 sK1-GNRs) (Fig. 3d). As a control to check
164 whether rotation of the GNR polarization is coupled to helical orbiting of the supertwist
165 of the microtubules or not, we studied GNRs coated with *rat* kinesin dimers dK1-GNRs,
166 which faithfully track protofilaments[6] rather than side-stepping. Polarization angle of
167 these dK1-GNRs did not exhibit unidirectional rotation along a long-pitch helical path in
168 our observation (Fig. 3e). These data indicate that periodic oscillations of the intensity of
169 polarized light scattered by kinesin-GNRs within the sample plane only occur for motor
170 teams that step along the short-pitch helical path.
171
172 **Helical and yaw-axis rotations of kinesin-coated GNRs.** Our GNR motility assays
173 revealed that the polarization of KIF1-, ZEN4-, and sK1-GNRs rotated periodically whilst
174 moving along a helical trajectory towards microtubule plus ends. Our results are well
175 explained by a model in which a kinesin-coated GNR unidirectionally rotates 180° about
176 its short (yaw) axis in one period of short-pitch helical motion around the microtubule
177 long axis (Supplementary movie 2). In this model, the time trajectories of the GNR angle
178 in the X–Y-plane are given by

179 $$\arctan\left[\cos(\omega_{\mathrm{roll}}t)\cdot\tan\left(\varphi+\omega_{\mathrm{yaw}}t\right)\right]$$

180 where ω_{yaw} and ω_{roll} $(=\pm 2\omega_{\mathrm{yaw}})$ are the angular velocities of yawing and rolling of
181 a kinesin-coated GNR on the microtubule, respectively and φ is defined by the relative
182 angle to the microtubule axis when the kinesin-coated GNR is at the top position of its

183 helical trajectory (Methods). Three types of observed rotations of the polarization angle
184 (counterclockwise, oscillatory, and clockwise rotations) are reproduced by our proposed
185 model depending on the initial-phase angles (φ) of the kinesin-coated GNR. For example,
186 rotations of the GNR polarization, as viewed from above the sample plane, are
187 counterclockwise at $\varphi = 0°$, oscillatory at $\varphi = 45°$ and 135°, and clockwise at $\varphi = 90°$ (Fig.
188 4 and Fig. S5a. See also Supplementary movie 2 and 3). Note that when the kinesin-
189 coated GNR moves along a helical path without yawing, rotation of the GNR polarization
190 is also oscillatory (Fig. 4 bottom and Fig. S5b. See also Supplementary movie 4). In this
191 model, the GNR yawing direction is also a determinant of apparent rotational patterns of
192 the GNR polarization in the sample plane. Pearson's correlation coefficient between the
193 *Y*-displacement and the angle of the kinesin-GNR is negative in the case of the clockwise
194 yawing, while the correlation coefficient of the counter-clockwise yawing is positive (Fig.
195 4 and Fig. S5a). Estimated by the correlation coefficient between the *Y*-displacement and
196 the polarization angle, 8 out of 13 KIF1-GNRs, 5 out of 13 ZEN4-GNRs, and 3 out of 5
197 sK1-GNR exhibited clockwise yawing, whilst 5 out of 13 KIF1-GNRs, 8 out of 13 ZEN4-
198 GNRs, and 2 out of 5 sK1-GNR counterclockwise yawing. The directionalities of yawing
199 of these kinesin-coated GNRs were not significantly different from an equal probability
200 using binomial test (p-values > 0.5 for KIF-GNR, ZEN4-GNR, and sK1-GNR).
201 Our proposed model, in which kinesin-GNRs rotate around their yaw axes as they move
202 along and around the microtubule long axis, predicts that immobilized kinesin-GNRs
203 might drive rotation of an overlying short microtubule about both its long and short axes.
204 To test the rotational motility of the kinesin-GNRs during translation, we performed the

205 surface-gliding assay for ZEN4-GNRs, in which ZEN4-GNR particles were sparsely
206 attached on the glass surface (3~8 particles per 100 μm^2) (Methods). We found indeed
207 that short microtubules (<~2 μm) slid until only their ends were in contact, and then
208 unidirectionally rotated on ZEN4-GNRs (Fig. 5 and Supplementary movie 5). In the
209 geometry of observation images, we observed both counterclockwise rotation (n = 4
210 microtubules) and clockwise rotation (n = 4 microtubules). These observations also
211 support a model in which kinesin-coated GNRs moving along a microtubule are driven
212 to undergo both helical and yaw-axis rotations.

Discussion

We developed the GNR motility assay and harnessed it to analyses cargo rotations driven by teams of single-headed KIF1A, dimeric ZEN-4, and single-headed kinesin-1. For all 3 kinesins, ~ 20% of the kinesin-coated GNRs showed periodic fluctuation of the GNR polarization signal, phase locked to the orbit of the GNR around the microtubule, over multiple orbital periods. For the remaining ~80% of records, we did not observe periodic variation in the GNR polarization signals. Where we did observe periodic fluctuation in the GNR polarization signals, we always saw phase-locking to the orbit of the GNR around the microtubule axis. Our observations reveal unidirectional yawing (rotation of the team) as a new mode of motility in three different types of kinesin teams.

We found that the polarization and helix pitches were comparable among KIF1-, ZEN4- and sK1-GNRs (0.7~0.8 μm) ($p > 0.05$ for adjusted pairwise comparisons using Welch's t-test with the Holm method), despite substantial differences in their forward velocities ($p < 0.01$ for adjusted pairwise comparisons using Welch's t-test with the Holm method). The helix pitch is given by $P = 2\pi V_X/\omega_{Helix}$, where P is the pitch size, V_X is the forward velocity, and ω_{Helix} is the angular velocity in the *Y–Z*-plane. We see that the forward velocities are different among KIF1-, ZEN4-, and sK1-GNRs but the pitches are equal. The ratios of V_X to ω_{Helix} are thus almost equal. This means that the angular velocity of helical motion is directly proportional to the forward velocity for all our kinesin-coated GNRs, suggesting that the off-axis component is intrinsic to each stroke, and independent of the rate of stroking.

This relationship can be well modeled by a 2D noise-driven ratchet mechanism, as proposed by Mitra *et al.* for single-headed KIF1A[19]. Based on this mechanism, we now consider how yawing of the kinesin-coated GNRs might influence its motility. Since a kinesin-coated GNR rotated 180° about its yaw axis in one period of a helical trajectory with the helix pitch of about 700 nm, the GNR rotates 2° ≈ 180°/(700 nm/8 nm) with 8 nm of forward displacement, which is equivalent to the length of the tubulin dimer. The 2° rotation generates at most ±1 nm ≈ ±20~34 nm × tan(2°) of lateral displacements of the kinesin molecules bound on the GNR (40 nm in diameter and 68 nm in length) (Fig. 6a). Lateral displacement (d) of 1 nm is equivalent to 0.2 ≈ 1 nm/5.1 nm[29] in the asymmetry factor (α) toward the off-axis, which would be sufficient to influence the noise-driven ratchet mechanism (Fig. 6b). A recent discussion by Mitra *et al.* indicates that around 1 μm of a helix pitch is reproduced by the 2D Brownian ratchet model with a slight off-axis asymmetry (α_Y = 0.53) relative to the on-axis asymmetry (α_X = 0.27)[19].

We evaluated the off-axis fluxes of three particles differing in their starting positions for diffusion ($-d, 0, +d$) in the noise-driven ratchet model with asymmetry potentials (α) after $1/\gamma$ units of time[30] (Methods):

$$J_0 = \frac{\gamma}{4}\left\{\mathrm{erfc}\left[\frac{\alpha}{2}\sqrt{\gamma}\right] - \mathrm{erfc}\left[\frac{1-\alpha}{2}\sqrt{\gamma}\right]\right\}$$

$$J_{\pm d} = \frac{\gamma}{4}\left\{\mathrm{erfc}\left[\frac{\alpha \mp d}{2}\sqrt{\gamma}\right] - \mathrm{erfc}\left[\frac{1-\alpha \pm d}{2}\sqrt{\gamma}\right]\right\}$$

where J_0 represents the flux of particles starting diffusion at 0 and $J_{\pm d}$ represents the flux of particles starting diffusion at $\pm d$. In calculations with α = 0.53 and γ = 160 s^{-1} (Methods), the absolute values of J_{-d} and J_{+d} increased with d along a sigmoidal

curve and the net flux, $J_{-d} + J_0 + J_{+d}$ described the convex downward function of which the value reached a minimum at d = 0.5 (Fig. 6c and 6d). Importantly, the slight displacement (d < 0.2) is sufficient to cause biased flux because $|J_{-d}|$ is much larger than $|J_{+d}|$ (Fig. 6c, inset). These suggest that unidirectional rotation of a motor-coated cargo enhances the sideward bindings of motor molecules toward the biased direction.

To explore the consequences of combined rotational and helical motion of kinesin-coated GNRs, we performed Monte Carlo simulations of the two-state noise-driven ratchet model. In this simulation, multiple particles, which are linked to a rigid body cargo with a spring, stochastically take biased forward and/or sideward steps on the 2D lattice and generate torque to twist the spring and then rotate the cargo when taking a step (Fig. 7). Based on the force- and moment-balance equations, the cargo moves and rotates around the center of the joint points connecting the particles in the attached state (Fig. 7a and Methods). Additionally, the twist angle ($\Delta\theta$) of the cargo driven by the torque generated by the particles taking a step is given by $\Delta\theta = \left(N_{\mathrm{step}}\theta_{\mathrm{step}} + b_\theta\right)/N_{\mathrm{on}}$, where N_{step} is the number of particles taking a step and generating a torque in a unit of time; N_{on} is the number of particles bound to the rail in the unit of time; b_θ is the rotational diffusion of the cargo with a normal distribution with zero mean and a standard deviation of σ_θ; θ_{step} is the twist angle of the spring driven by the torque T_{step} generated by the single particle, assuming that the twist angle θ_{step} is proportional to the torque T_{step} (Methods). Note that the rotational diffusion of the cargo (b_θ) is negligible for the particle formation in Figure 7a (Methods).

First, we optimized the parameters for the biased forward and sideward movement of

277 the cargo without torque generation (θ_{step}= 0), matching the ~0.8-μm helix pitch of
278 KIF1A and ZEN-4 in the gliding assay, which is the ratio of forward steps to leftward
279 steps (~100/13) (Fig. 7b). We note that the simulation without torque generation often
280 showed unidirectional rotation of the cargo, but the period of rotation was irregular and
281 uncorrelated with the 13-lattice period of the *Y*-displacements modeled as the 13-
282 protofilament microtubule. We then performed the simulation with torque generation.
283 When θ_{step} was approximately −3° to −4°, the cargo exhibited periodical clockwise
284 rotation and the period of rotation closely matched the 13-lattice period (Fig. 7c and Fig.
285 S6). Correlation between counterclockwise rotation and sideward movement of the cargo
286 was also reproduced when θ_{step} was +4° (Fig. S7). The lateral displacement in a
287 calculation time in the presence of torque (θ_{step}= −4°) increased about 1.3-fold, compared
288 with that in the absence of torque (θ_{step}= 0°), which is consistent with the analysis by the
289 noise-driven ratchet model indicating that unidirectional rotation of a motor-coated cargo
290 enhances the sideward bindings of motor molecules toward the biased direction (Fig. 6d).
291 In this simulation, lower number or lower density of particles result in weaker
292 correlations between the *Y*-displacement and the rotation trajectories (Fig. S8), suggesting
293 that the formation of particles on the cargo are also critical for the rotation motility of a
294 kinesin team. Less frequent observation of the kinesin-GNRs showing periodic
295 fluctuation in the GNR polarization signals might be caused by heterogeneous formations
296 of kinesin molecules on the kinesin-GNRs. Also, in the GNR assay experiments, each
297 kinesin-coated GNR exhibited specific directionality of yawing, which is consistent with
298 previous single-molecule measurements for the kinesin-1 dimer[9]. Although the detailed

299 mechanism of directional yawing of a kinesin team remains unclear, not only the
300 conformational changes in the motor domain but also the formation of kinesin molecules
301 on the GNR and further the configuration of the kinesin-GNR and the microtubule might
302 be involved.

303 A recent single-molecule study of the kinesin-1 dimer construct revealed that it
304 unidirectionally rotates the stalk domain by ~1° with 8-nm steps at high ATP conditions
305 and in the presence of an external force[9]. Therefore, the estimated θ_{step} of 4° might be
306 reasonable especially in the absence of an external force. Previous structural studies of
307 kinesin-1 and KIF1A revealed that rearrangement in the motor domain from the pre-
308 stroke state to the post-stroke state contains rotational motions of the subdomains[31–33]. A
309 torque-generation property may be built into the kinesin motor domain (Supplementary
310 discussion). Furthermore, the neck-to-tail region is critical for torque transmission from
311 the head domain to the cargo. In the case of ZEN-4, its neck domain contains a non-
312 canonical long sequence; however, high-speed AFM imaging of a ZEN-4 dimer revealed
313 a distinctive globular mass in the neck region[34]. Thus, the non-canonical neck-domain of
314 ZEN-4 may be a stiffness component rather than a flexible linker.

315 Previous studies proposed that sideward stepping of kinesins and dynein allows them
316 to bypass roadblocks on a microtubule[6–8,11,13,35]. We performed Monte Carlo simulations
317 of bypassing of a roadblock with various multiple-motor motilities, especially changing
318 the two parameters: the off-axis asymmetry, α_Y, and the torque generation, θ_{step} (Fig.
319 7d and Methods). The simulation results in the case of α_Y = 0.58 and θ_{step} = 0 showed
320 that the sideward movement allowed motors to avoid the roadblock (Fig. 7d, second from

321 the left), whereas the motors without off-axis asymmetry (α_Y = 0.5 and θ_{step} = 0) failed
322 to bypass it within the calculation time (Fig. 7d, the most left). Moreover, the simulation
323 results in the case of α_Y = 0.5 and θ_{step} = −4° indicate that the rotational motility also
324 helps motors avoid the obstacle (Fig. 7d, second from the right). Interestingly, the motors
325 with off-axis asymmetry (α_Y = 0.58) and torque generation (θ_{step} = −4°) exhibited a
326 'spin move' (i.e., a combination of spinning and sideward motion), and further increased
327 the probability of bypassing the obstacle (Fig. 7d, the most right). The evasion time by
328 the spin move was 2.6-fold faster than that by only sideward stepping. These simulations
329 thus suggest that the spin move of a kinesin team will help sustained transport of a cargo
330 in situations where the microtubule lattice is crowded with microtubule associated
331 proteins, motor proteins, and other lattice-binders.

332 In summary, the GNR motility assay of single-headed KIF1A, dimeric ZEN-4, and
333 single-headed kinesin-1 revealed that kinesin-coated GNRs unidirectionally rotated
334 around their yaw axis, phase-locked with their helical orbit of the microtubules.
335 Theoretical analyses with a noise-driven 2D ratchet model and Monte Carlo simulations
336 showed that unidirectional rotation enhances the biased sideward movement of kinesin-
337 bound cargo. Our results reveal that in kinesin teams, the production of torque drives not
338 only orbital motion of the kinesin team around the microtubule axis, but also coupled
339 yaw-axis rotation of the team and its attached cargo. We propose based on quantitative
340 simulations that this combination of properties enables cargos bound to multiple kinesins
341 more efficiently to bypass roadblocks. Our work provides new insights into the structural
342 basis of kinesin motor stepping[33,36] and into the implications of their translational and

343 rotational degrees of freedom for their cellular function[37].

METHODS

Gold nanorod imaging. Figure 1a shows a schematic drawing of the laser dark-field microscope system used for gold nanorod (GNR) imaging. The laser dark-field optical system was constructed on an inverted microscope (Ti; Nikon, Tokyo, Japan), equipped with variable-angle epi-illumination[21,22] and a custom-built perforated dichroic mirror (PDM) (Sigma Koki, Tokyo, Japan). The PDM had an elliptical hole (short axis = 6 mm; long axis = 8.5 mm) at its center position, which made a circular window when viewed from the optical axis. The scattered light from the GNRs was transmitted through this central circular window. Illumination was performed using a 635-nm diode laser (MRL-III-635L-10mW; CNI laser, Changchun, China), which was further attenuated by neutral density filters (ND) and converted to circularly polarized light by a quarter-wave plate (WPQ-6328-4M; Sigma Koki, Tokyo, Japan). The collimated and circularly polarized incident beam was focused by a lens (L1 in Fig.1a, f = 220 mm) onto the back focal plane of the objective lens (PlanApo N, 60×, NA 1.42; Olympus, Tokyo, Japan). GNR images were obtained by laser dark-field imaging using highly inclined illumination with nearly total internal reflection angle. The back focal plane was focused outside a camera port of the microscope with an achromatic lens (L3 in Fig.1a, f = 60 mm) to make an equivalent back focal plane for constructing the optics for polarization measurements and 3D tracking.

For polarization measurements, the scattered light from a GNR illuminated by polarized incident beam was further split into two orthogonally polarized components by a polarization beam displacer (BD40; Thorlabs, Tokyo, Japan), which was set in the

366 optical path between the relay optics constructed by two lenses (L3 (f = 60 mm) and L4
367 (f = 120 mm) in Fig.1a)[38]. Two separated and polarized light beams were imaged as two
368 spots on a CMOS camera (LDH2500; Digimo, Tokyo, Japan). The orientations of the two
369 orthogonally separated polarization components of the beam displacer were diagonal
370 relative to the transmission axis of the polarization filter. For angular calibration, a linear
371 polarizer was additionally set at the position between L2 and L3 and rotated from 0° to
372 180° in 10° intervals (Fig. 1b).

373 For 3D tracking, concave and convex cylindrical lenses (CnC (f = –200 mm) and CvC
374 (f = 200 nm)) were set in front of the camera[24]. The interval between CnC and CvC was
375 13 mm. Calibration of 3D tracking along the Z-axis was performed by moving the
376 objective in 50-nm intervals (Fig. S1), using a custom-built stage equipped with a pulse
377 motor (SGSP-13ACT; Sigma Koki, Tokyo, Japan) and a controller (QT-CM2; Chuo
378 Precision Industrial, Tokyo, Japan). We analyzed the widths of the GNR spots along the
379 X-axis (S_X) and Y-axis (S_Y) obtained by 2D-Gaussian fits. The calibration factor for the z-
380 displacement obtained from the ratio of S_Y to S_X was 0.98 μm/ratio.

381 The temperature of the sample stage was controlled using a custom-built water-
382 circulating temperature control system. Image acquisition in the GNR motility assay was
383 performed at 100 frames/s with the commercial software for the CMOS camera (Digimo,
384 Tokyo, Japan). The data were saved as eight-bit AVI files. The effective pixel size of the
385 detector was 42 nm. Image analysis and further analyses were performed using custom
386 software written in LabVIEW (National instruments, Tokyo, Japan).

387

388 **Polarization measurements.** For polarization measurements, the scattered light from a
389 GNR illuminated by polarized incident beam was split into two polarized components by
390 the polarization beam displacer as mentioned above. Thus, the intensities of two polarized
391 GNR spots as functions of the GNR orientation (θ) are expressed by

392 $$I_{\text{bottom}} = I_0 \cdot \cos^2(\theta + \beta) \cdot \cos^2(\theta + \beta - \gamma) \cdot + b$$

393 $$I_{\text{upper}} = I_0 \cdot \cos^2(\theta + \beta) \cdot \cos^2(\theta + \beta - \gamma + 90) + b$$

394 where I_0 is the amplitude; θ is the GNR orientation in the sample plane; β and γ are
395 phase angles of polarization of the incident beam in the sample plane and the beam
396 displacer, respectively; and b is the background intensity. The observed intensity
397 profiles in Fig. 1b were well fitted by these functions with I_0 = 127.5 ± 3.3, β = 99.3°
398 ± 0.8°, γ = 45.3° ± 0.7°, and b = 19.5 ± 0.9. GNR angles in the sample plane were
399 obtained by fitting an ellipse function to the plot of the degree of polarization
400 $(I_{\text{bottom}} - I_{\text{upper}})/(I_{\text{bottom}} + I_{\text{upper}})$ as a function of the summed-intensity (I_{bottom} +
401 I_{upper}), as shown in Fig. 1b.
402
403 **Kinesin constructs.** In all kinesin constructs used in this study, the functional sequence
404 Avi-His, which consists of the Avi-tag (GLNDIFEAQKIEWHE) for biotinylation and the
405 6×His-tag for histidine-affinity purification, was fused to the C-terminus of truncated
406 kinesin domains. For the monomeric KIF1A construct, the fragment of *human* KIF1A (1–
407 366 amino acid residues (AAs)) obtained from a *human* cDNA library was cloned into
408 eGFP-Avi-His/pColdIII plasmids. eGFP stabilized the solubility of the truncated KIF1A
409 sample. In addition, for the surface-gliding assay of the KIF1A construct, we used the

410 construct of *human* KIF1A (1–366 AAs) cloned into mRuby-Zdk1-His/pColdIII plasmids.
411 For the dimeric ZEN-4 construct, the fragment of *C. elegans* ZEN-4 (1–555 AAs)
412 obtained from CBD-TEV-ZEN4/pGEX-6p plasmids[34] was cloned into Avi-His/pET32a
413 plasmids. For the monomeric and dimeric kinesin-1 constructs, the fragments of *rat*
414 kinesin-1 (1–340 AAs and 1–430 AAs for the monomeric and dimeric constructs[27],
415 respectively) were cloned into Avi-His/pColdIII plasmids. All constructs were verified by
416 DNA sequencing.
417
418 **Expression and purification of kinesin.** For expression and purification of the kinesin
419 constructs, the proteins were expressed in *Escherichia coli* strain BL21 Star (DE3) cells
420 using 0.4 mM Isopropyl-β-D-thiogalactopyranoside (IPTG) (Sigma) for 9 to12 hours at
421 20 °C. The collected cells were lysed in lysis buffer (50 mM potassium phosphate; pH
422 7.4, 350 mM NaCl, 1 mM $MgCl_2$, 10 μM ATP, 1 mM DTT, 0.1% Tween20, 10% glycerol,
423 protease inhibitors, 50 mM imidazole) and sonicated in iced water for 15 minutes. The
424 bacterial lysate was centrifuged for 20 minutes at 260,000*g* at 4 °C to remove cell debris
425 and insoluble proteins. The clarified supernatant was purified with the His-tag affinity by
426 chromatography with a HisTrap HP Ni^{2+}sepharose column (GE Healthcare). The
427 collected peak fraction was further purified through a HiTrap desalting column (GE
428 Healthcare) to exchange the buffer (20 mM potassium phosphate; pH 7.4, 1 mM $MgCl_2$,
429 1 mM DTT, 10 μM ATP) containing 80 mM NaCl for the KIF1A and the kinesin-1
430 constructs, or 250 mM NaCl for the Zen-4 construct.
431 For the KIF1A construct, we further purified the active proteins based on their affinity

432 for microtubules[39]. KIF1A and microtubules were mixed and incubated for 15 minutes in
433 the presence of 1 mM AMPPNP. The mixture was centrifuged for 20 minutes at 260,000*g*
434 at 25 °C to remove unbound KIF1A molecules. The pellet was resuspended in ATP-
435 containing buffer (20 mM PIPES-KOH; pH 7.4, 5 mM $MgCl_2$, 10 mM potassium acetate,
436 250 mM NaCl, 20 μM paclitaxel, 5 mM ATP) and incubated for 15 minutes at 23 °C for
437 detachment of KIF1A molecules from the microtubules. Microtubules were removed by
438 centrifugation (260,000*g*, 15 minutes, 23 °C).
439 The purified proteins were flash-frozen and stored in liquid nitrogen. The concentration
440 of proteins was estimated using the Bradford method with the use of BSA as a standard.
441
442 **Purification of tubulin.** Tubulin was purified from porcine brains through four cycles of
443 temperature-regulated polymerization and depolymerization in a high-molarity PIPES
444 buffer to remove contaminating MAPs[40]. The purified tubulin was flash-frozen and stored
445 in liquid nitrogen.
446
447 **Preparation of Cy5-microtubules.** Tubulin stock solution (~6 mg mL^{-1}, 50 μL) and
448 Cy5-labelled tubulin solution (~20 mg mL^{-1}, 1 μL, ~50% labelled) were mixed on ice
449 and then diluted twofold with chilled BRB80 buffer (80 mM PIPES-KOH; pH 6.8, 1 mM
450 $MgCl_2$, 1 mM EGTA). One microliter each of GTP (100 mM), and $MgCl_2$ (100 mM) was
451 added to the diluted tubulin solution. The tubulin solution was incubated at 37 °C for 1
452 hour for polymerization and stabilized with 20 μM paclitaxel. The Cy5-microtubules
453 were further purified by centrifugation[39]. Ray *et al.* reported that polymerization in PIPES

454 buffer results in ~60% of 14-protofilament microtubules and ~30% of 13-protofilament
455 microtubules[41].
456
457 **Preparation of protein-G-coated beads and streptavidin-coated gold nanorods.** For
458 preparation of protein G-coated beads, carboxylate-modified fluorescent microbeads (0.5
459 μm; Thermo Fisher Scientific, USA) were diluted in the activation buffer (100 mM MES;
460 pH 6.0). EDC and sulfo-NHS were added to the bead solution and incubated for 15
461 minutes at room temperature. The beads were then washed with 100 mM HEPES buffer
462 at pH 8.0. Protein-G was then added to the bead solution and reacted for 2 hours at room
463 temperature. Any unreacted amine reactive groups were quenched by adding excess
464 glycine. Excess proteins were removed by centrifugation (21,000*g*, 15 minutes, 23 °C).
465 The beads were resuspended in BRB80 buffer.
466 For preparation of streptavidin-coated GNRs, biotin-labelled GNRs (5 nM) (C12-40-
467 600-TB; Nanopartz, CO, USA) and streptavidin (5 mg mL^{-1}) were mixed. After 15
468 minutes' incubation, excess streptavidin was removed by centrifugation (4,000*g*, 3
469 minutes, 23 °C) and then the pellet was resuspended in Milli-Q water and sonicated for 2
470 s. The procedure for removing excess streptavidin was repeated twice.
471
472 **GNR motility assays.** Streptavidin-coated GNR (2 μL, 5 nM) and kinesin sample (2 μL,
473 1–2 μM) were mixed and incubated for at least 15 minutes at room temperature. For the
474 assay of KIF1A, 2 μL of 0.2% Tween20 was further added to the mixture of kinesin and
475 GNR. For the assay for ZEN-4, 0.5 μL of 5 M NaCl and 2 μL of 0.2% Tween20 were

476 further added to the mixture of kinesin and GNR.

477 A flow chamber (sample volume of about 5 μL) was prepared using two coverslips (24
478 mm × 32 mm and 18 mm × 18 mm) stuck by double-sided tape. Protein-G-coated bead
479 solution was nonspecifically absorbed to the coverslip. After 3 minutes' incubation, the
480 flow chamber was washed with 20 μL of 1 mg mL^{-1} BSA and further incubated for 3
481 minutes. The flow chamber was washed with 20 μL of BRB80. Then, 10 μL of 20 μg
482 mL^{-1} anti-β-tubulin antibody solution (sc-58884; Santa Cruz, USA) was flowed to the
483 flow chamber. After 3 minutes' incubation, the flow chamber was washed with 20 μL of
484 BRB80. Then, 10 μL of Cy5-lablled microtubule solution (~2 μM tubulin concentration)
485 was flowed into the flow chamber such that the microtubules bound to the beads (Fig.
486 1c). After 3 minutes' incubation, the flow chamber was washed with 20 μL of 1 mg mL^{-1}
487 casein. After 3 minutes' incubation, the flow chamber was washed with 20 μL of the
488 motility buffer (20 mM PIPES-KOH; pH 7.4, 4 mM $MgCl_2$ and 10 mM potassium
489 acetate) containing the kinesin-coated GNRs (~100 pM), ATP (2 mM), the ATP
490 regeneration system (0.8 mg mL^{-1} creatine kinase, 10 mM creatine phosphate), the
491 oxygen scavenger system (3 mg mL^{-1} glucose, 50 U mL^{-1} glucose oxidase, 1200 U mL^{-1}
492 catalase), and 1 mg mL^{-1} casein. The GNR assays were performed at 27 °C. Image
493 acquisition was performed at 100 frames s^{-1}.

494

495 **Surface-gliding assays for KIF1A with QD-coated microtubules.** Qdot525 (QD)-
496 coated and Cy5-labelled microtubules were prepared as previously described[18]. The
497 surface-gliding assays were performed in flow chambers assembled from two coverslips

498 attached using double-sided tapes. Before the assay, kinesin stock solution was diluted to
499 1 μM with motility buffer. Five microliters of a 5 mg mL^{-1} solution of protein G (Sigma-
500 Aldrich, Tokyo, Japan) was added to the flow chamber (about 5 μL). After 5 minutes'
501 incubation, the flow chamber was washed with 20 μL of BRB80 buffer, followed by
502 another 5 minutes of incubation with 5 μL of 0.05 mg mL^{-1} anti-His-tag antibody. The
503 flow chamber was washed with 20 μL of BRB80 buffer, and then 5 μL of 0.5 mg mL^{-1}
504 casein solution was added. After 5 minutes' incubation, the flow chamber was washed
505 with 20 μL of BRB80 buffer. Then, 10 μL of KIF1A solution (1 μM) was added to the
506 flow chamber. The flow chamber was then washed with 20 μL of BRB80 after 5 minutes'
507 incubation, and 20 μL of QD-coated microtubule solution (0.05–0.1 μM tubulin) was
508 added to the flow chamber. Finally, the flow chamber was washed with 20 μL of BRB80
509 buffer after 5 minutes' incubation, and 20 μL of motility buffer containing 3 mM ATP, 20
510 μM paclitaxel, 0.5% β-mercaptoethanol, 0.25 mg mL^{-1} casein, ATP regeneration and
511 oxygen scavenger systems were added. Fluorescent images of the QD- and Cy5-labelled
512 microtubules were captured using TIRF microscopy at 25 °C. Corkscrewing pitches in
513 the surface-gliding assay were determined by measuring the longitudinal displacement of
514 the QDs in each period of oscillation of the lateral displacement along the microtubule
515 axis.
516
517 **Surface-gliding assays for ZEN4-GNR.** Preparations of Cy5-labelled microtubules and
518 ZEN4-GNR were prepared as described above. Surface-gliding assays were performed
519 in flow chambers assembled from two coverslips attached using double-sided tape. The

520 ZEN4-GNR solution was diluted to ~50 pM with motility buffer and added to the flow
521 chamber (about 5 μL). After 5 minutes' incubation, the flow chamber was washed with
522 20 μL of BRB80 buffer, followed by 5 minutes' incubation with 10 μL of 0.5 mg mL^{-1}
523 casein solution. The flow chamber was then washed with 20 μL of BRB80 buffer, and 20
524 μL of Cy5-labelled microtubule solution (2 mM ATP, Cy5-labelled microtubules, 0.25 mg
525 mL^{-1} casein, and ATP regeneration and oxygen scavenger systems in motility buffer)
526 were added. The assays were performed at 27 °C. Image acquisition of the Cy5-labelled
527 microtubules was performed at 10 frames s^{-1}.
528
529 **Quantification and statistical analysis.** Polarization and position data of the observed
530 kinesin-coated GNRs were obtained by image analysis with software written in
531 LabVIEW (National instruments, Tokyo, Japan). Velocities of the kinesin-coated GNRs
532 were determined by fitting the trace of the longitudinal displacement along the
533 microtubule axis (*X*-direction) with a linear function. Rotation and helix pitches in the
534 GNR assays were determined by measuring the *X*-displacements in the periods of
535 oscillations of the angle- and *Y*-trajectories, respectively. Statistical hypothesis testing
536 was performed using R statistical software.
537
538 **Correction of the measured pitch.** The measured pitch (P_{Measured}) comprised two
539 helical elements: the helix pitch exerted by motors (P_{Motor}) without supertwist of the
540 microtubule, and the supertwist of the microtubule depending on the number of the
541 protofilaments (P_{MT}). P_{Measured} is given by

$$\frac{1}{P_{\mathrm{Measured}}} = \frac{1}{P_{\mathrm{Motor}}} + \frac{1}{P_{\mathrm{MT}}}$$

The P_{MT} of 12-, 13-, and 14-protofilament microtubules is estimated to be about −3.4, −24.8, and 6.8 μm, respectively (we assign a positive value to the pitch in the left-handed helix)[41]. When the absolute value of P_{Measured} is much smaller than the absolute value of P_{MT} (< ~1 μm), P_{Motor} is not appreciably changed by the supertwist (Fig. S4).

Mathematical model of helical and rotational motion of a kinesin-coated GNR on a microtubule. The GNR motility assay revealed that KIF1-, ZEN4-, and sK1-GNRs unidirectionally rotate about the GNR's short axis, moving along the left-handed helix track. The helix track of the center position of a GNR is given by

$$h(x, y, z) = (vt, a \cdot \cos(\pi/2 - \omega_{\mathrm{Helix}} t), a \cdot \sin(\pi/2 - \omega_{\mathrm{Helix}} t))$$

where v is the translational velocity along the *x*-axis, ω_{Helix} is the angular velocity in the *Y*–*Z*-plane, and a is the radius of the helix. Assuming that the long axis of the GNR is parallel to the *X*–*Y*-plane under the initial conditions, the initial position matrix consisting of the tip, center, and end positions of the GNR is given by

$$I(\mathrm{tip}, \mathrm{center}, \mathrm{end}) = \begin{pmatrix} r \cdot \cos(\varphi) & 0 & r \cdot \cos(\varphi + \pi) \\ r \cdot \sin(\varphi) & 0 & r \cdot \sin(\varphi + \pi) \\ 0 & 0 & 0 \end{pmatrix}$$

where r is the radius along the long axis of the GNR and φ is its phase angle. Because a kinesin-coated GNR unidirectionally rotates about its short axis and further around the microtubule, the resultant rotation comprises yawing and rolling. We assume that a kinesin-coated GNR would not rotate about the pitch axis. Matrices of yawing and rolling

are given by

$$R_{\mathrm{Yaw}}(\omega_{\mathrm{Yaw}}t) = \begin{pmatrix} \cos(\omega_{\mathrm{Yaw}}t) & -\sin(\omega_{\mathrm{Yaw}}t) & 0 \\ \sin(\omega_{\mathrm{Yaw}}t) & \cos(\omega_{\mathrm{Yaw}}t) & 0 \\ 0 & 0 & 1 \end{pmatrix}$$

$$R_{\mathrm{Roll}}(\omega_{\mathrm{Roll}}t) = \begin{pmatrix} 1 & 0 & 0 \\ 0 & \cos(\omega_{\mathrm{Roll}}t) & -\sin(\omega_{\mathrm{Roll}}t) \\ 0 & \sin(\omega_{\mathrm{Roll}}t) & \cos(\omega_{\mathrm{Roll}}t) \end{pmatrix}$$

where ω_{Yaw} and ω_{Roll} are the angular velocities of yawing and rolling, respectively. Taken together, the helical and rotational trajectory of a motor-coated GNR is written as

$$R_{\mathrm{Roll}}R_{\mathrm{Yaw}}I + h$$

Thus, the time trajectory of the GNR orientation in the *X*–*Y*-plane is given by

$$\arctan[\cos(\omega_{\mathrm{Roll}}t) \cdot \tan(\varphi + \omega_{\mathrm{Yaw}}t)]$$

Our analyses indicate that kinesin-coated GNRs rotate 180° in one period of the helix. This is the case of $\omega_{\mathrm{helix}} = \omega_{\mathrm{roll}} = \pm 2\omega_{\mathrm{Yaw}}$. The calculated helical and rotational trajectories of a kinesin-coated GNR and the time trajectories of the GNR orientation with different phase angles are shown in Fig. 4, Fig. S5, and Supplementary movies 2–4.

Evaluation of particle flux in the noise-driven ratchet model. The previous study by Astumian and Bier[30] clarified the particle flux in the two-state, noise-driven ratchet model. Following their discussions, we evaluated the particle flux for different start positions, assuming that sideward translations ($\pm d$) of motors takes place owing to the rotation of their cargo (see Fig. 6a). In the two-state ratchet model, when the barrier moves to the down state, the particles start to diffuse. The probability density function of a diffusing particle at the start position of $+d$ in the *X*-direction is given by

$$P_{+d}(x;t) = \frac{1}{2\sqrt{\pi t}} \exp\left[-\frac{(x-d)^2}{4t}\right].$$

After $1/\gamma$ units of time, the probability that the particle is located to the right of α is given by $\int_{\alpha}^{\infty} P_{+d}(x;1/\gamma)dx = \frac{\gamma}{4}\mathrm{erfc}\left[\frac{\alpha-d}{2}\sqrt{\gamma}\right]$ and the probability that it on the left of $-(1-\alpha)$ is $\int_{-\infty}^{-(1-\alpha)} P_{+d}(x;1/\gamma)dx = \frac{\gamma}{4}\mathrm{erfc}\left[\frac{1-\alpha+d}{2}\sqrt{\gamma}\right]$. The particle flux, J_{+d} is thus given by

$$J_{+d} = \frac{\gamma}{4}\left\{\mathrm{erfc}\left[\frac{\alpha-d}{2}\sqrt{\gamma}\right] - \mathrm{erfc}\left[\frac{1-\alpha+d}{2}\sqrt{\gamma}\right]\right\}.$$

Similarly, J_{-d} and J_0 are also obtained, as detailed in main text.

Following the probability density function of a diffusing particle, the standard deviation of diffusion, σ, is given by $\sqrt{2/\gamma}$. When γ is 160 s^{-1}, $\sigma \approx 0.11$, which is equal to the value of σ in the Monte Carlo simulations (see below).

Monte Carlo simulations. We performed Monte Carlo simulations to model the observed rotational and helical motion. In the simulation, each particle is linked to a rigid body as a cargo with a spring (spring constant, k) and the joint points linking the particles and the cargo are fixed. The particles stochastically attach and dissociate from the rail (on-time constant, τ_{on}; off-time constant, τ_{off}). A detached particle diffuses around the joint point (standard deviation of diffusion, σ) in the *X*–*Y*-plane. When the diffusing particle overrides the asymmetric barrier (asymmetric factors, α_X and α_Y) at the last time of diffusion, the particle takes a step in the *X*–*Y*-direction. The force- and moment-balance equations are given by $\sum_i^{N_{\mathrm{on}}} k\overrightarrow{d_i} = 0$ and $\sum_i^{N_{\mathrm{on}}} k\overrightarrow{d_i} \times \overrightarrow{l_i} = 0$, where k is the

spring constant; $\overrightarrow{d_i}$ is an extension vector of the spring of the i-th particle that is bound to the rail; $\overrightarrow{l_i}$ is the position vector of the i-th joint relative to the center of the joint points connecting the particles that are bound to the rail; and N_{on} is the number of the particles bound to the rail. In the simulation, $\overrightarrow{d_i}$ is the displacement between the i-th particle and the i-th joint position. Furthermore, torque rotating the cargo is exerted by the particle when it takes a step. A twist angle ($\Delta\theta$) of the cargo by the torque generated by the particle taking a step is given by $\Delta\theta = \left(N_{\mathrm{step}}\theta_{\mathrm{step}} + b_\theta\right)/N_{\mathrm{on}}$ and $\theta_{\mathrm{step}} = T_{\mathrm{step}}L/KG$, where N_{step} is the number of particles taking steps; N_{on} is the number of particles bound to the rail; θ_{step} is the twist angle of the spring; b_θ is the rotational diffusion of the cargo as a normal distribution with zero mean and a standard deviation of σ_θ; T_{step} is the torque force generated by the single particle; L is the length of the spring; G is the modulus of rigidity of the spring; and K is the polar moment of inertia of area of the spring. We thus assume that the twist angle θ_{step} is proportional to the torque force T_{step}. The value of θ_{step} as the torque force was given in the simulation. After calculating the force and moment balance equations, the cargo additionally rotates $\Delta\theta$ degrees about the center of the joint points connecting the particles that are bound to the rail.

A roadblock in the simulation allowed the off-state particles to diffuse above it, whereas the on-state particles could not attach to the roadblock except at its edges. We used the roadblock with a width of 40 lattices and a length of 30 lattices.

The simulation was developed in LabVIEW (National Instruments). The values for the parameters used in the simulation were: τ_{on} = 40 units of time; τ_{off} = 10 units of time;

α_X = 0.12 units of lattice size; α_Y = 0.58 units of lattice size; σ = 0.11 units of lattice size; θ_{step} = 4°; $b_\theta = 0$. Note that the value of σ was determined by the evaluation of particle flux in the noise-driven ratchet model mentioned in the previous subsection, and that the rotational diffusion of the cargo (b_θ) is negligible for the particle formation in Figure 7a, compared the results of Fig. 7c and Fig. S8b.

Reproducibility

Data for all the GNR assay experiments were acquired during at least three independent experimental days.

Reporting summary

Further information on research design is available in the Nature Research Reporting Summary linked to this article.

Data availability

The data that support this study are available from the corresponding author upon reasonable request.

Code availability

LabVIEW source code and executable software for the Monte Carlo simulations used in this study are available https://github.com/MitsuSGW/MonteCarlo-MotorTeam-Sim.git

Acknowledgement

CBD-TEV-ZEN4/pGEX-6p plasmid was a gift from Prof. Masanori Mishima. We thank Prof. TOYOSHIMA Y. Yoko and SAITO Kei for critical discussion; Adam Brotchie, PhD, from Edanz Group (www.edanzediting.com/ac) for editing a draft of this manuscript. This work is supported by KAKENHI (JP19K06593, JP19H03190 to M.S.; JP20K06635 to J.Y.) from MEXT, Japan (Ministry of Education, Culture, Sports, Science and Technology), by MEXT KAKENHI Grant-in-Aid for Scientific Research on Innovative Areas (JP21H00386, JP21H05868 to J.Y.), by Research Foundation for Opto-Science and Technology, Japan to M.S.

655 **REFERENCES**

656 1. Vale, R. D. The Molecular Motor Toolbox for Intracellular Transport. *Cell* **112**,
657 467–480 (2003).
658 2. Hirokawa, N., Noda, Y., Tanaka, Y. & Niwa, S. Kinesin superfamily motor
659 proteins and intracellular transport. *Nat. Rev. Mol. Cell Biol.* **10**, 682–696 (2009).
660 3. Verhey, K. J. & Hammond, J. W. Traffic control: Regulation of kinesin motors.
661 *Nat. Rev. Mol. Cell Biol.* **10**, 765–777 (2009).
662 4. Yajima, J., Mizutani, K. & Nishizaka, T. A torque component present in mitotic
663 kinesin Eg5 revealed by three-dimensional tracking. *Nat. Struct. Mol. Biol.* **15**,
664 1119–21 (2008).
665 5. Nitzsche, B., Ruhnow, F. & Diez, S. Quantum-dot-assisted characterization of
666 microtubule rotations during cargo transport. *Nat. Nanotechnol.* **3**, 552–556
667 (2008).
668 6. Brunnbauer, M. *et al.* Torque Generation of Kinesin Motors Is Governed by the
669 Stability of the Neck Domain. *Mol. Cell* **46**, 147–158 (2012).
670 7. Bugiel, M. & Schäffer, E. Three-Dimensional Optical Tweezers Tracking
671 Resolves Random Sideward Steps of the Kinesin-8 Kip3. *Biophys. J.* **115**, 1993–
672 2002 (2018).
673 8. Mitra, A., Ruhnow, F., Girardo, S. & Diez, S. Directionally biased sidestepping
674 of Kip3/kinesin-8 is regulated by ATP waiting time and motor–microtubule
675 interaction strength. *Proc. Natl. Acad. Sci.* **115**, E7950–E7959 (2018).
676 9. Ramaiya, A., Roy, B., Bugiel, M. & Schäffer, E. Kinesin rotates unidirectionally

677 and generates torque while walking on microtubules. *Proc. Natl. Acad. Sci.* **114**,
678 10894–10899 (2017).
679 10. Yildiz, A., Tomishige, M., Gennerich, A. & Vale, R. D. Intramolecular strain
680 coordinates kinesin stepping behavior along microtubules. *Cell* **134**, 1030–41
681 (2008).
682 11. Maruyama, Y. *et al.* CYK4 relaxes the bias in the off-axis motion by MKLP1
683 kinesin-6. *Commun. Biol.* **4**, (2021).
684 12. Pan, X., Acar, S. & Scholey, J. M. Torque generation by one of the motor
685 subunits of heterotrimeric kinesin-2. *Biochem. Biophys. Res. Commun.* **401**, 53–
686 57 (2010).
687 13. Bormuth, V. *et al.* The highly processive kinesin-8, Kip3, switches microtubule
688 protofilaments with a bias toward the left. *Biophys. J.* **103**, L4–L6 (2012).
689 14. Walker, R. A., Salmon, E. D. & Endow, S. A. The Drosophila claret segregation
690 protein is a minus-end directed motor molecule. *Nature* **347**, 780–782 (1990).
691 15. Nitzsche, B. *et al.* Working stroke of the kinesin-14, ncd, comprises two substeps
692 of different direction. *Proc. Natl. Acad. Sci.* **113**, E6582–E6589 (2016).
693 16. Mitra, A. *et al.* Kinesin-14 motors drive a right-handed helical motion of
694 antiparallel microtubules around each other. *Nat. Commun.* **11**, 1–11 (2020).
695 17. Yajima, J. & Cross, R. A. A Torque Component in the Kinesin-1 Power Stroke.
696 *Nat. Chem. Biol.* **1**, 338–341 (2005).
697 18. Yamagishi, M., Fujimura, S., Sugawa, M., Nishizaka, T. & Yajima, J. N-terminal
698 β-strand of single-headed kinesin-1 can modulate the off-axis force-generation

699 and resultant rotation pitch. *Cytoskeleton* **77**, 351–361 (2020).

700 19. Mitra, A. *et al.* A Brownian ratchet model explains the biased sidestepping of
701 single-headed kinesin-3 KIF1A. *Biophys. J.* **8**, 1–9 (2019).

702 20. Yamagishi, M., Maruyama, Y., Sugawa, M. & Yajima, J. Characterization of the
703 motility of monomeric kinesin-5/Cin8. *Biochem. Biophys. Res. Commun.* **555**,
704 115–120 (2021).

705 21. Konopka, C. A. & Bednarek, S. Y. Variable-angle epifluorescence microscopy:
706 A new way to look at protein dynamics in the plant cell cortex. *Plant J.* **53**, 186–
707 196 (2008).

708 22. Tokunaga, M., Imamoto, N. & Sakata-Sogawa, K. Highly inclined thin
709 illumination enables clear single-molecule imaging in cells. *Nat. Methods* **5**,
710 159–61 (2008).

711 23. Ueno, H. *et al.* Simple dark-field microscopy with nanometer spatial precision
712 and microsecond temporal resolution. *Biophys. J.* **98**, 2014–2023 (2010).

713 24. Watanabe, T. M. *et al.* Four-dimensional spatial nanometry of single particles in
714 living cells using polarized quantum rods. *Biophys. J.* **105**, 555–564 (2013).

715 25. Okada, Y. & Hirokawa, N. A processive single-headed motor: Kinesin
716 superfamily protein KIF1A. *Science (80-.).* **283**, 1152–1157 (1999).

717 26. Hutterer, A., Glotzer, M. & Mishima, M. Clustering of Centralspindlin Is
718 Essential for Its Accumulation to the Central Spindle and the Midbody. *Curr.*
719 *Biol.* **19**, 2043–2049 (2009).

720 27. Yajima, J., Alonso, M. C., Cross, R. a & Toyoshima, Y. Y. Direct long-term

721 observation of kinesin processivity at low load. *Curr. Biol.* **12**, 301–6 (2002).

722 28. Berliner, E., Young, E. C., Anderson, K., Mahtani, H. K. & Gelles, J. Failure of a
723 single-headed kinesin to track parallel to microtubule protofilaments. *Nature* **373**,
724 718–721 (1995).

725 29. Chrétien, D. & Fuller, S. D. Microtubules switch occasionally into unfavorable
726 configurations during elongation. *J. Mol. Biol.* **298**, 663–676 (2000).

727 30. Astumian, R. D. & Bier, M. Fluctuation driven ratchets: Molecular motors. *Phys.*
728 *Rev. Lett.* **72**, 1766–1769 (1994).

729 31. Kikkawa, M. & Hirokawa, N. High-resolution cryo-EM maps show the
730 nucleotide binding pocket of KIF1A in open and closed conformations. *EMBO J.*
731 **25**, 4187–4194 (2006).

732 32. Cao, L. *et al.* The structure of apo-kinesin bound to tubulin links the nucleotide
733 cycle to movement. *Nat. Commun.* **5**, (2014).

734 33. Hwang, W., Lang, M. J. & Karplus, M. Kinesin motility is driven by subdomain
735 dynamics. *Elife* **6**, 1–25 (2017).

736 34. Davies, T. *et al.* CYK4 Promotes Antiparallel Microtubule Bundling by
737 Optimizing MKLP1 Neck Conformation. *PLoS Biol.* **13**, 1–26 (2015).

738 35. Can, S., Dewitt, M. a & Yildiz, A. Bidirectional helical motility of cytoplasmic
739 dynein around microtubules. *Elife* e03205 (2014) doi:10.7554/eLife.03205.

740 36. Hwang, W. & Karplus, M. Structural basis for power stroke vs . Brownian
741 ratchet mechanisms of motor proteins. (2019) doi:10.1073/pnas.1818589116.

742 37. Kaplan, L., Ierokomos, A., Chowdary, P., Bryant, Z. & Cui, B. Rotation of

743 endosomes demonstrates coordination of molecular motors during axonal
744 transport. *Sci. Adv.* **4**, (2018).
745 38. Enoki, S. *et al.* High-Speed Angle-Resolved Imaging of a Single Gold Nanorod
746 with Microsecond Temporal Resolution and One-Degree Angle Precision. *Anal.*
747 *Chem.* **87**, 2079–2086 (2015).
748 39. Yamagishi, M. *et al.* Structural Basis of Backwards Motion in Kinesin-1-
749 Kinesin-14 Chimera: Implication for Kinesin-14 Motility. *Structure* **24**, 1322–
750 1334 (2016).
751 40. Castoldi, M. & Popov, A. V. Purification of brain tubulin through two cycles of
752 polymerization-depolymerization in a high-molarity buffer. *Protein Expr. Purif.*
753 **32**, 83–8 (2003).
754 41. Ray, S., Meyhöfer, E., Milligan, R. A. & Howard, J. Kinesin follows the
755 microtubule's protofilament axis. *J. Cell Biol.* **121**, 1083–1093 (1993).
756

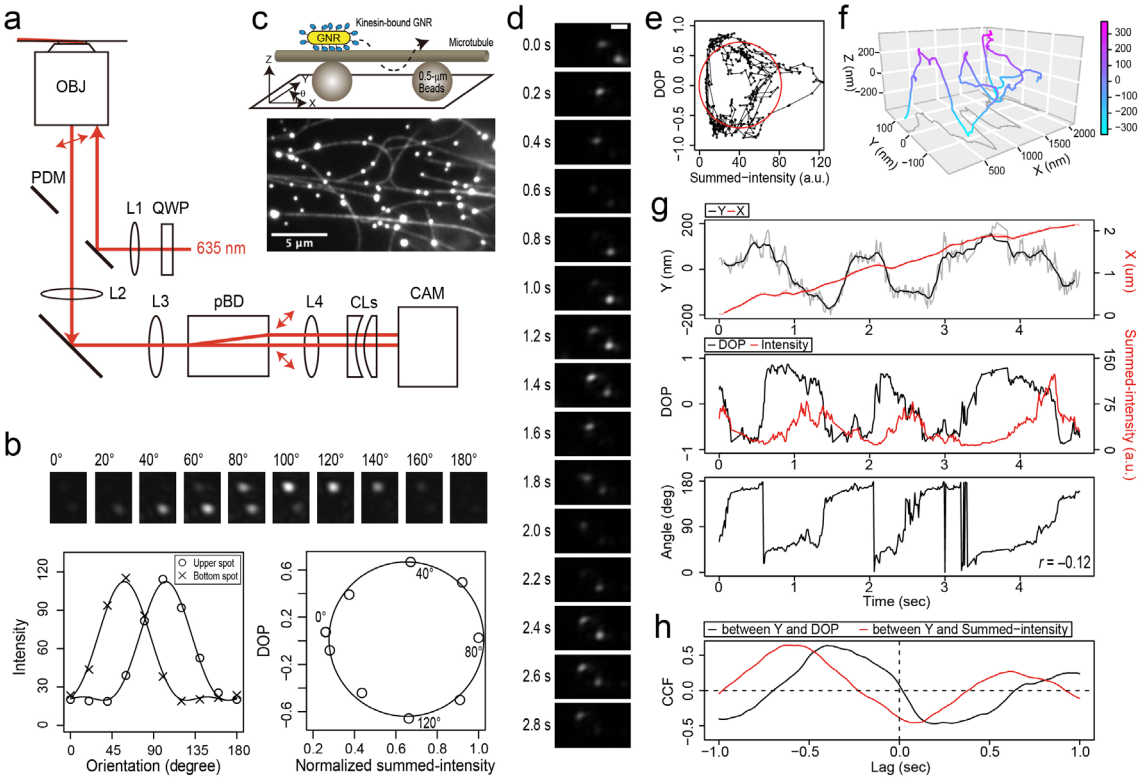

Figure 1. GNR motility assay for KIF1A. (**a**) Schematic drawing of the optics for 3D tracking and polarization measurements of a gold nanorod (GNR) using laser dark-field imaging with variable-angle epi-illumination. OBJ, objective lens; PDM, perforated dichroic mirror; QWP, quadruple wave plate; pBD, polarizing beam displacer; CL, cylindrical lens; CAM, CMOS camera; L, lens. (**b**) Calibration for polarization measurements. (upper) Series of pairs of scattered-light spots of microbeads (0.1 μm) modulated by a polarizer, which was located in front of L3, for emulating GNR spots with various orientations on the surface. (lower left) Intensity profiles of a pair of scattered-light spots ($I_{\mathrm{bottom}}, I_{\mathrm{upper}}$) shown in the upper images. The plots of I_{bottom} and I_{upper} were fitted by intensity functions of the GNR orientation. (lower right) Degree of polarization (DOP) $(I_{\mathrm{bottom}} - I_{\mathrm{upper}})/(I_{\mathrm{bottom}} + I_{\mathrm{upper}})$ as a function of the normalized summed-intensity of two scattered-light spots ($I_{\mathrm{bottom}} + I_{\mathrm{upper}}$). See

770 Methods for details. (**c**) (top) Schematic drawing of the GNR motility assay in which a
771 kinesin-coated GNR moves along a microtubule suspended with fluorescent microbeads
772 (0.5 μm) attached to a glass substrate. (bottom) Fluorescence image of Cy5-labelled
773 microtubules suspended on fluorescent microbeads. The bright spots are the fluorescent
774 microbeads. (**d**) Montage of scattered-light images of one KIF1A-coated GNR (KIF1-
775 GNR) moving around a microtubule every 0.2 s in the presence of 2 mM ATP. The frame
776 rate was 100 frames/s. Scale bar, 2 μm. **(e)** DOP as a function of the summed-intensity of
777 the two KIF1-GNR spots shown in (d). The red line represents an ellipse fit. (**f**) 3D
778 trajectory of the KIF1-GNR shown in (d) through a moving-average filter of 15 frames.
779 (**g**) The time trajectories of the *X*- and *Y*-displacements (upper), the DOP and summed-
780 intensity of the two spots (middle), and the estimated angle (bottom) of KIF1-GNR shown
781 in (d). The value of *r* is Pearson's correlation coefficient between the *Y*-displacement and
782 the angle. **(h)** Cross-correlation functions (CCFs) between the *Y*-displacement and the
783 polarization signals.

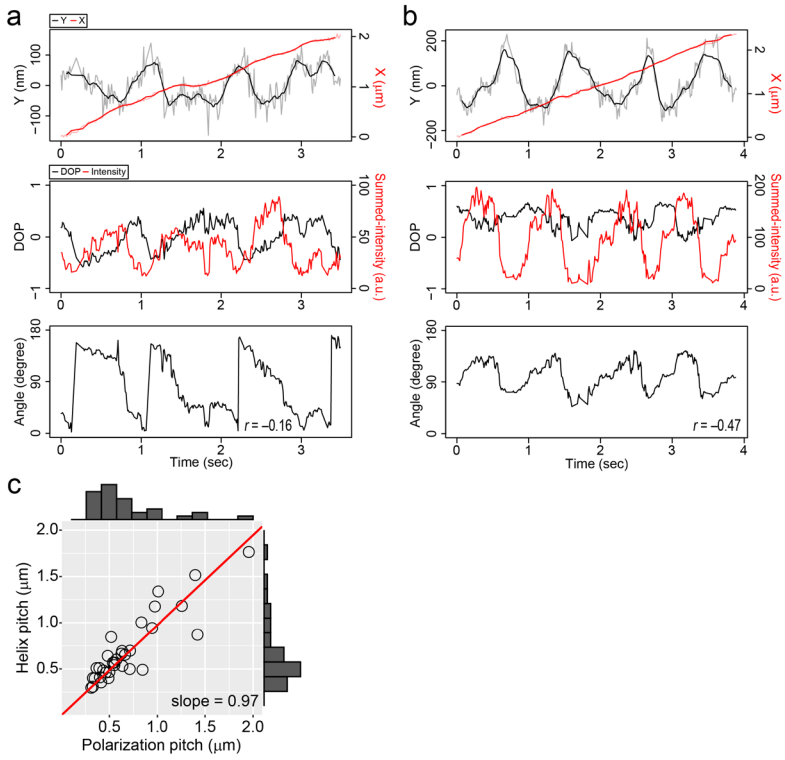

Figure 2. Typical data of the GNR motility assay for KIF1A. **(a, b)** The time trajectories of the *X*- and *Y*-displacements (upper), the degree of polarization (DOP) and summed-intensities of the two spots (middle), and the estimated angles (bottom) of KIF1-GNRs. The time trajectories of the polarization in the image plane show clockwise rotation (a) and oscillatory rotation (b). The value of *r* is Pearson's correlation coefficient between the *Y*-displacement and the angle. **(c)** Distribution of the helix and polarization pitches of KIF1-GNRs. The helix and polarization pitches are the displacements during one period of the *Y*-displacement and the polarization fluctuations, respectively. The red line represents a linear fit ($y = ax$) of which the slope (a) is 0.97 (R^2 = 0.95).

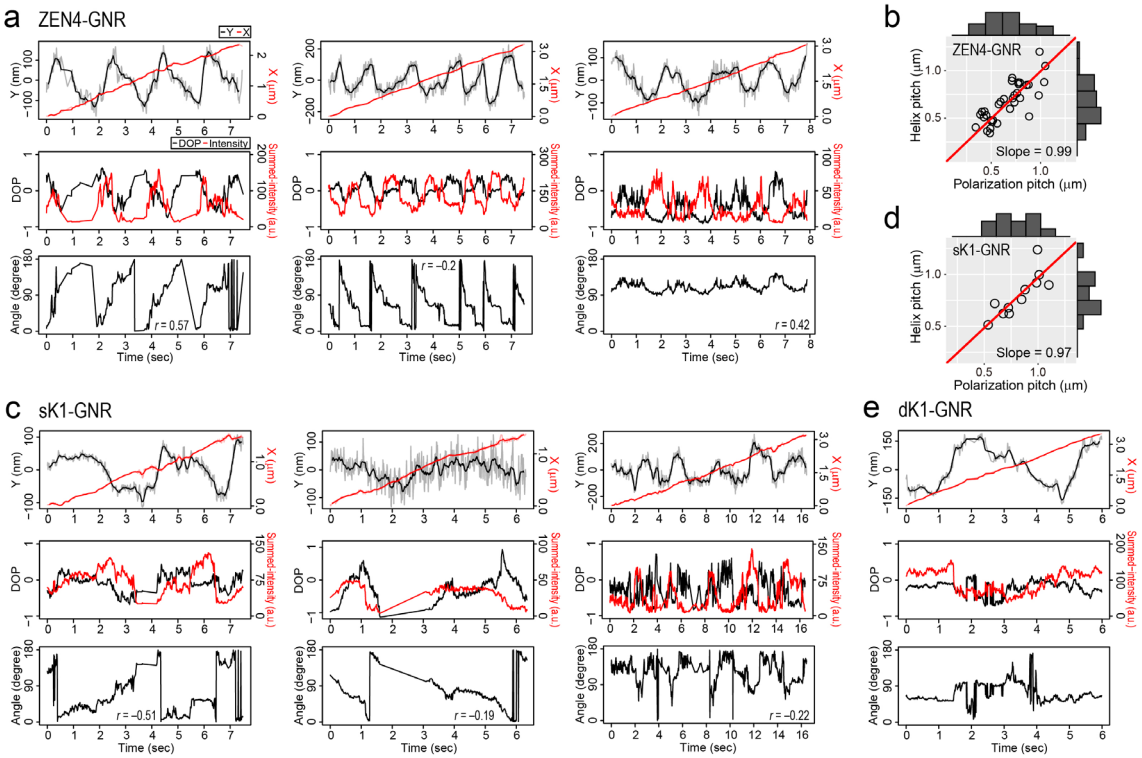

Figure 3. GNR motility assay for ZEN-4 and kinesin-1. **(a, c)** Typical time trajectories of the *X*- and *Y*-displacements (upper), the degree of polarization (DOP) and summed-intensity of the two spots (middle), and the estimated angles (bottom) of ZEN-4-coated gold nanorods (ZEN4-GNRs) (a) and single-headed kinesin-1 coated GNRs (sK1-GNRs) (c). The three trajectories represent counterclockwise (left), clockwise (middle), and oscillatory (right) rotations of the GNR polarization in the sample plane. The value of *r* is Pearson's correlation coefficient between the *Y*-displacement and the angle. **(b, d)** Distribution of the helix and polarization pitches of ZEN4-GNRs (b) and sK1-GNRs (d). The red lines represent linear fits ($y = ax$) of which the slopes (a) are 0.99 ($R^2 = 0.97$) (b) and 0.97 ($R^2 = 0.98$) (d). **(e)** Typical time trajectories of the *X*- and *Y*-displacements (upper), the DOP and summed-intensity of the two spots (middle), and the estimated angle (bottom) of double-headed kinesin-1 coated GNRs (dK1-GNRs).

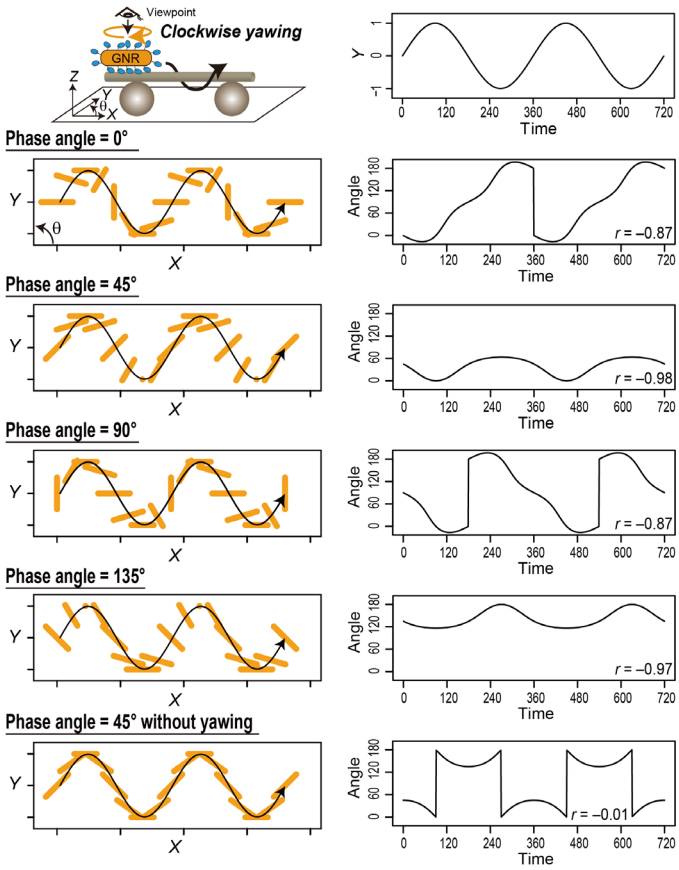

Figure 4. Interpretation of the observed polarization and translational movement of the kinesin-coated gold nanorods (GNRs). (Left) Montage of the projection images of a GNR in the *X*-*Y* plane, obtained by a mathematical model of a motor-coated GNR rotating 180° about its yaw axis in the clockwise yawing, in one period of the helical motion. (Right) Time trajectories of the *Y*-displacement and angle of a motor-coated GNR with different initial phase angles (φ = 0° (180°), 45°, 90°, and 135°). The value of *r* is Pearson's correlation coefficients between the *Y*-displacement and the angle. Trajectories of a motor-coated GNR in cases of the counterclockwise yawing and non-yawing are shown in Fig. S5. See also Supplementary movies 2–4.

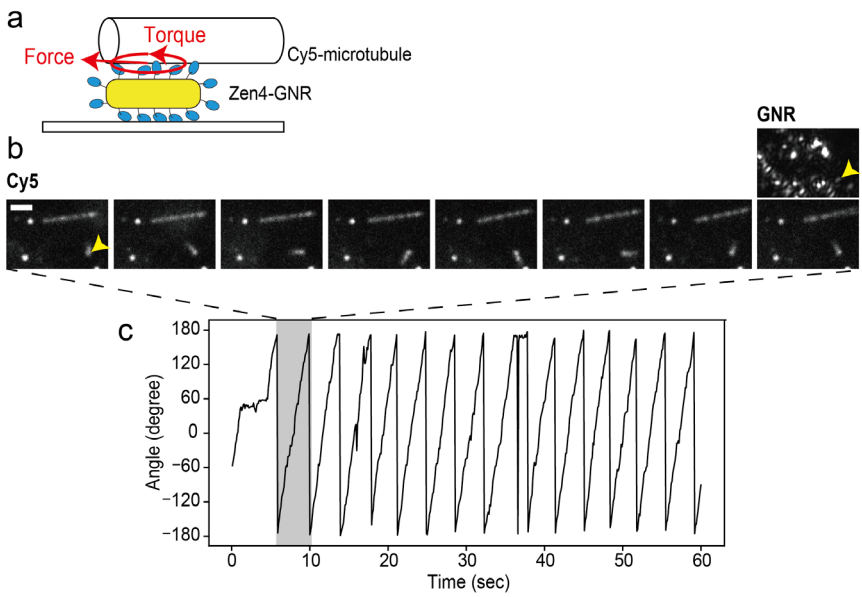

Figure 5. Surface-gliding assay for ZEN-4 coated gold nanorods (ZEN4-GNRs). (**a**) Schematic drawing of the surface-gliding assay, whereby the generation of force and torque rotate a Cy5-labelled microtubule (Cy5-microtubule) on the ZEN4-GNR. (**b**) Montage of fluorescence images of Cy5-microtubules every six frames (600 ms), showing that the short Cy5-microtubule continuously rotated (yellow arrowhead). Scale bar, 2 μm. GNR image of the same region-of-interest of the Cy5 images is also shown (right upper). (**c**) Time trajectory of the microtube orientation.

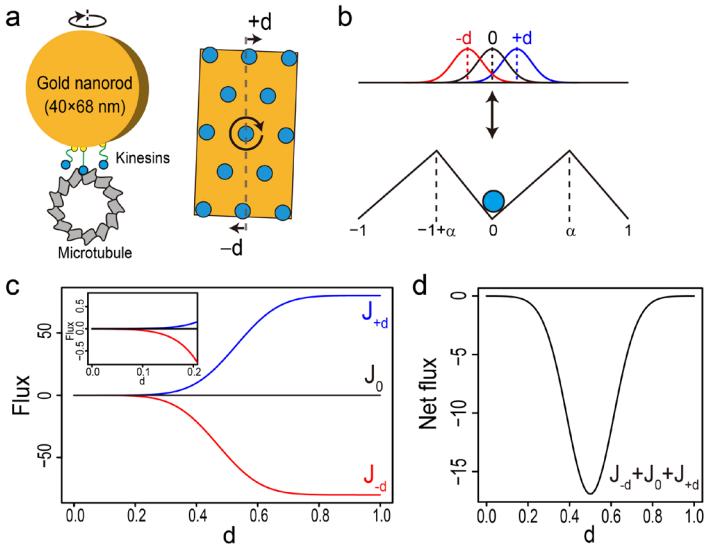

Figure 6. Mechanistic model for the clockwise rotation and helical motion of kinesin-coated gold nanorods (GNRs). (**a**) By rotation of the GNR, motors in the posterior and anterior positions relative to the rotation axis move laterally with displacement of $\pm d$. (**b**) This situation can be modeled using the noise-driven ratchet model with asymmetry potentials (α) and three different starting positions of the particles ($-d$, 0, $+d$). (**c, d**) Fluxes of three particles at the starting positions of diffusion in the noise-driven ratchet with asymmetry potentials after $1/\gamma$ units of time (Methods). (**c**) Fluxes of three particles as a function of d with $\alpha = 0.53$ and $\gamma = 160$ s^{-1}. (**d**) Net flux, $J_{-d} + J_0 + J_{+d}$, as a function of d.

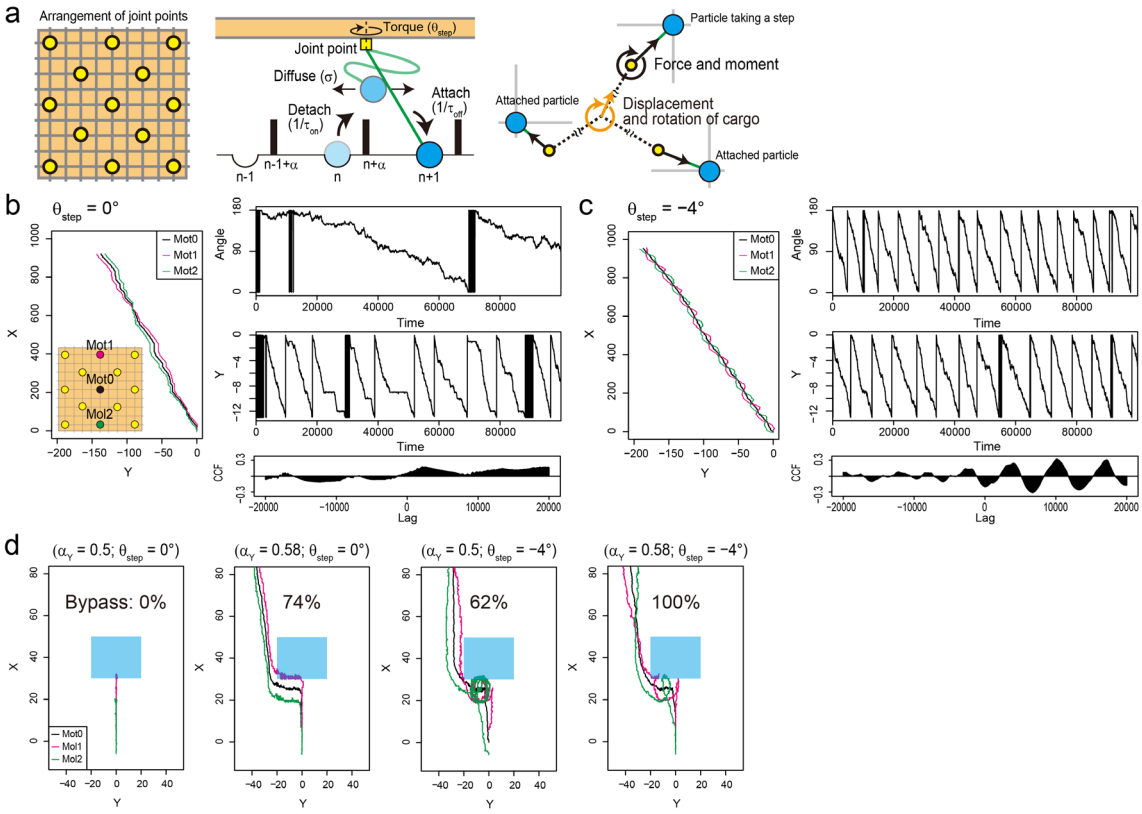

Figure 7. Monte Carlo simulation of the model for kinesin-coated gold nanorods. (**a**) Schematic description of the model. Particles (blue balls) are linked to a rigid body as a cargo (orange square) with a spring (green line), and the formation of their joint points (yellow circle or square) are fixed relative to the cargo axis. Particles repeatedly detach and attach to the 2D lattice rail with rate constants of $1/\tau_{\mathrm{on}}$ and $1/\tau_{\mathrm{off}}$, respectively. A detached particle diffuses around the joint points with a standard deviation of σ. When the particle passes over the barrier with an asymmetric factor (α), at the last time of diffusion, it will attach to the neighboring binding site and generate torque, twisting the spring by θ_{step}. Translational and rotational motions of the cargo are driven by the balances of force and moment (torque). (**b, c**) Simulation results without and with torque generation ($\theta_{\mathrm{step}} = 0°$ in (**b**) and $\theta_{\mathrm{step}} = -4°$ in (**c**)). The parameters are specified in

Methods. (left) Typical *X*–*Y*-trajectories of three representative particles (black, magenta, and green filled circles) represent biased forward, sideward and rotational motions of the cargo. (right) Time trajectories of the angle and *Y*-displacement, and their cross-correlation function (CCF). The axes of the angle and the *Y*-direction are converted to 180°- and 13-lattice periods, respectively. **(d)** Typical examples of simulations of bypassing an obstacle. α_Y and θ_{step} are the sideward asymmetric and torque parameters, respectively (see the main text). The percentages represent the probabilities of success in bypassing the obstacle (blue rectangle) within a calculation time of 55,000 and out of 300 trials.